Application of 3D Ambient Noise Tomography for Void Detection

Khiem T. Tran, Ph.D.[1]; and Yao Wang[2]

[1]Associate Professor, Dept. of Civil and Coastal Engineering, Univ. of Florida, Gainesville, FL. Email: ttk@ufl.edu
[2]Ph.D. Student, Dept. of Civil and Coastal Engineering, Univ. of Florida, Gainesville, FL. Email: wangyao@ufl.edu

ABSTRACT

A first-time application of 3D ambient noise tomography (3D ANT) method is presented for detection of deep voids. The method is based on the solution of 3D P-SV elastic wave equations and adjoint-state optimization to directly invert experimental cross-correlation functions (CCF) for extraction of S-wave velocity (Vs) structure. The main advantage of this approach is that it does not rely on assumptions of energy balance and far-field waves as required by methods using characteristics of Green's function (GF). Instead, the source power-spectrum density is inverted to account for source distribution (location and energy), which allows to exploit full information content of all available CCFs from ambient noise recordings. The 3D ANT capability in detecting deep voids is investigated at a test site in southern Florida. For the field experiment, 72 vertical geophones of 4.5-Hz resonance were deployed in a 4 × 18 grid over 9.0 × 76.5 m area on the ground surface to record noise data for 34 min. The CCFs extracted from the noise recordings have good energy at 5–20 Hz and a consistent wave propagation pattern for the entire test area. The inverted result reveals that the 3D ANT was able to image a large deep void at 28- to 44-m depth, which is generally consistent with results from invasive SPTs.

INTRODUCTION

Underground voids pose significant risk to the safety of infrastructure such as public transportation systems and residential buildings. They must be detected and monitored consistently, particularly in areas that are suffering from numerous voids. Surface-based geophysical methods such as the ground penetrating radar (GPR), electrical resistivity tomography (ERT), and active-source seismic full-waveform inversion (FWI) are often used for void detection. They can scan large volumes of subsurface materials at lower cost than invasive techniques. The FWI is an efficient approach for void imaging, and typically provides higher characterized resolutions with depths than those of GPR or ERT (Tran et al. 2013). However, detection of deep voids (> 20 m depth) is difficult, because the surface-based wavefields highly attenuate with penetration depth. Mirzanejad et al. (2021) showed that low-frequency components (< 10 Hz) are required for imaging such deep voids. In that study, they used a strong active source (340 kg drop weight) to generate seismic wavefields down to 5 Hz to image a 30-m depth void. As such strong sources are expensive, we aim to utilize the low-frequency ambient noise already present in the environment for deep void investigation.

Many ambient noise tomography (ANT) methods have been developed for site investigation at various depths from tens to hundreds of meters. Most of existing ANT methods invert dispersion characteristics (dispersion curve) of noise fields or Green's functions (GFs) (Louie, 2001; Di Giulio et al., 2006; Rosenblad and Li, 2009; Endrun et al., 2010; Moschetti et al., 2010;

Yang et al., 2011; Behm et al., 2016). These methods can provide deep 1D Vs profiles to depths of hundreds of meters. However, they cannot be used for detection of 3D voids due to the averaging effects of inverted Vs over the length of the sensor array and a depth of about one wavelength of analyzed data.

Recently, Wang et al. (2021) developed a 2D ANT method that directly invert cross-correlation functions (CCF) of traffic noise to extract 2D Vs profiles of roadway structures. It was successfully applied on field datasets for detection of voids under roadway. However, the 2D ANT method assumes that the wave propagation direction is mainly along the receiver line. The assumption is valid for traffic noise induced by vehicles passing along the receiver line, but it is not fully valid for cases of ambient noise arriving from various directions. To address the issue of wave propagation directions, Wang et al., (2023) developed a 3D ANT method that inverts both source distribution (location and energy) and Vs profiles from the CCF waveforms. Applying to field data, the 3D ANT has shown good capability in characterizing a 3D Vs profile of subsurface soils (Wang et al., 2023). In this study, we further investigate its capability in detecting voids with field experiment.

METHODOLOGY

The 3D ANT method (Wang et al., 2023) is used in this study for void detection. As the method has not been well stablished, it is briefly summarized herein. The 3D ANT consists of forward simulation and model updating. The forward simulation is based on the numerical solution of 3D P-SV elastic wave equations (Nguyen and Tran, 2018) for computing synthetic CCFs. Model updating is based on the adjoint-state optimization to minimize CCF residuals for extraction of material property.

Forward simulation

The time-domain CCF $C^{\alpha\beta}$ between two signals s^{α} and s^{β} at receivers α and β is explicitly computed by:

$$C^{\alpha\beta}(t) = \int s^{\alpha}(\tau) s^{\beta}(t+\tau) d\tau. \tag{1}$$

where t denotes time, and τ is time offset. However, it is not possible to explicitly simulate the seismograms s^{α} and s^{β} due to unknown source locations of ambient noise fields. Thus, we compute CCF implicitly (Sager et al., 2018, 2020; Wang et al., 2021) as:

$$C^{\alpha\beta}(t) = \frac{1}{2\pi} \int \int_{\Omega''} \int_{\Omega'} \mathrm{G}(\boldsymbol{x}^{\alpha}, \boldsymbol{x}', \omega)\, \mathrm{f}(\boldsymbol{x}', \omega)\, \mathrm{G}^{*}\left(\boldsymbol{x}^{\beta}, \boldsymbol{x}'', \omega\right) \mathrm{f}^{*}(\boldsymbol{x}'', \omega) \exp(i\omega t)\, d\Omega' \mathrm{d}\Omega''\, d\omega. \tag{2}$$

where ω is frequency, i is the imaginary unit, and the asterisk symbol denotes complex conjugate. Variables $\boldsymbol{x}'$ and $\boldsymbol{x}''$ are two arbitrary locations in the 3D domain Ω, and integrals $\int_{\Omega'} d\Omega'$ and $\int_{\Omega''} d\Omega''$ denote the integration over domain Ω twice, distinctively, $\mathrm{G}(\mathbf{x}^{\alpha}, \mathbf{x}, \omega)$ is the Green's function with the source located at $\mathbf{x}^{\alpha}$, and $\mathrm{f}(\mathbf{x}, \omega)$ is the source function. Assuming that the spatial correlation length of noise sources is shorter than the seismic wavelengths present in

the noise, the source terms can be approximated with a delta function (δ) in space and the source power spectrum density (PSD) $S(\boldsymbol{x}, \omega)$ (Wapenaar and Fokkema, 2006):

$$\mathrm{f}(\boldsymbol{x}', \omega)\, \mathrm{f}^*(\boldsymbol{x}'', \omega) = S(\boldsymbol{x}', \omega)\delta(\boldsymbol{x}' - \boldsymbol{x}''), \tag{3}$$

By its definition, the PSD is a field of scalar values that show the spatial location and the strength of sources. With this approximation, Equation 2 becomes:

$$\mathrm{C}^{\alpha\beta}(\mathrm{t}) = \frac{1}{2\pi} \int \int_{\Omega} \mathrm{G}(\mathbf{x}^{\alpha}, \mathbf{x}, \omega) \left[\mathrm{G}^*\left(\mathbf{x}^{\beta}, \mathbf{x}, \omega\right) S(\mathbf{x}, \omega)\right] \exp(\mathrm{i}\omega \mathrm{t})\, \mathrm{d}\mathbf{x}\mathrm{d}\omega, \tag{4}$$

and

$$\mathrm{C}^{\alpha\beta}(\omega) = \int_{\Omega} \mathrm{G}(\mathbf{x}^{\alpha}, \mathbf{x}, \omega) \left[\mathrm{G}^*\left(\mathbf{x}^{\beta}, \mathbf{x}, \omega\right) S(\mathbf{x}, \omega)\right] \mathrm{d}\mathbf{x}. \tag{5}$$

Equations (4) and (5) can be used to compute the CCF in the time and the frequency domain, respectively. Using Equation (5), the CCF is computed implicitly for a given noise source distribution (all noise events) instead of individual noise events. We compute the CCF between $\mathbf{x}^{\alpha}$ and $\mathbf{x}^{\beta}$ by performing the following steps:

1) Run two forward 3D wavefield propagation simulations to compute Green's functions $\mathrm{G}(\mathbf{x}^{\alpha}, \mathbf{x}, \omega)$ and $\mathrm{G}\left(\mathbf{x}^{\beta}, \mathbf{x}, \omega\right)$ with sources at $\mathbf{x}^{\alpha}$ and $\mathbf{x}^{\beta}$.
2) Multiply $\mathrm{G}(\mathbf{x}^{\alpha}, \mathbf{x}, \omega)$ with the complex conjugate $\mathrm{G}^*(\mathbf{x}^{\beta}, \mathbf{x}, \omega)$ and the noise source PSD $\mathrm{S}(\mathbf{x}, \omega)$. The noise source PSD is directly inverted from measured CCFs and $\mathrm{S}(\mathbf{x},\omega)$ is the same (average value) for all frequencies within a filtering band.
3) Sum over all grid points (integration over space $\mathbf{x}$) and transform the frequency-domain CCF to the time domain.

Adjoint-state inversion

The misfit (residual) between the observed and synthetic CCFs is computed as:

$$\delta C = C_{obs} - C_{syn}. \tag{6}$$

The objective function (E) is then defined as the L2-norm of the misfit:

$$\mathrm{E} = \frac{1}{2} \delta \mathrm{C}^{\mathrm{T}} \delta \mathrm{C} = \frac{1}{2} \sum_{\alpha} \int \mathrm{dt} \sum_{\beta} \delta \mathrm{C}^2. \tag{7}$$

To minimize the objective function, the PSD and Vs are both updated during inversion as:

$$\begin{cases} S^{p+1} = \| S^p + \theta_1 |K_s|_{L1} \|, \\ \mathrm{V_s^{p+1}} = \mathrm{V_s^p} + \theta_2 \delta \mathrm{V_s}. \end{cases} \tag{8}$$

where the index p denotes the iteration number. K_s and $\delta \mathrm{V_s}$ are gradients of the misfit E with respect to PSD and Vs, respectively [refer to Wang et al., (2023) for detailed calculation]. The

operator $|\circ|_{L1}$ is the L-1 normalization. The operator $\|\circ\|$ denotes a PSD magnitude normalization. This normalization neglects the negative values and maps the non-negative magnitude of the PSD to the range [0,1]. The step length θ_1 and θ_2 are positive scalers. The gradient δV_s is normalized by dividing its maximum magnitude. Via numerical trials, we use θ_1 equal to 0.05 (5% of the maximum normalized PSD) and θ_2 equal to 0.02 (2% of the maximum Vs of the current model during inversion.

FIELD EXPERIMENT

The field experimental site is at a bridge construction site in Miami, Florida, USA. The site (Figure 1) is in an urban area, and next to Highway I-395 and local roads. The site contains a known deep and large void identified via invasive standard penetration tests (SPT) and seismic active-source 3D FWI (Mirzanejad et al. 2021). For ambient noise recording for 3D ANT, due to limited space along the roadway, an array of 72 vertical 4.5-Hz geophones were deployed on an 18 × 4 grid of 4.5 m × 3 m spacing (Figure 2) on the ground surface and right above the void.

The geophone array is 76.5 m × 9 m (X×Y). The center of the void is located approximately at the center of the geophone array. The two SPT locations are denoted by red stars in Figure 2.

Figure 1. Miami highway bridge site

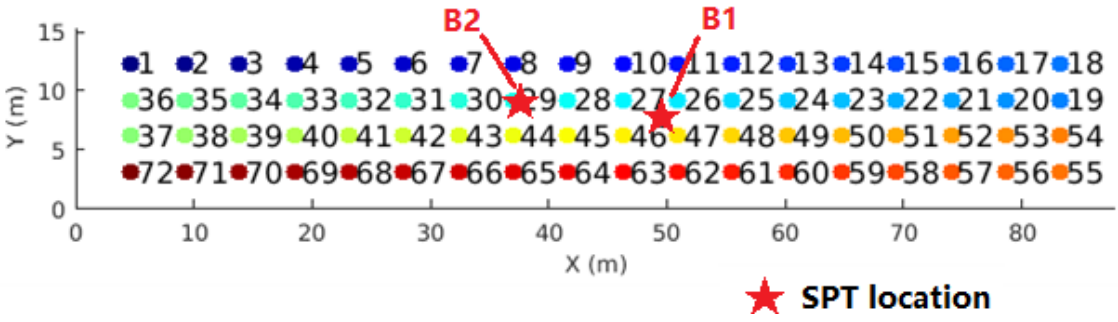

Figure 2. Test configuration at the Miami highway bridge site. Geophones are labeled with station numbers.

Seventeen noise records were collected and each one lasted for 120 seconds (34 minutes in total recorded data). The collected data contains abundant traffic-induced surface waves because of the high traffic volume around the site area. During the recording time, vehicles were frequently passing by, providing good signal strength for the traffic-induced surface waves. A sample noise record is displayed in Figure 3 with many traffic-induced seismic events (Figure 3a), and a clear surface-wave event highlighted with red dash lines (Figure 3b).

For data processing, the noise recording is filtered to keep low frequencies (< 20 Hz) and then divided into 0.3-second segments. It is noted that 0.3 second is long enough for surface waves passing through the geophone array. A longer segment can be used but may lead to the undesired source correlation issue (correlating wave events from different sources). The CCF between every station pair is calculated for each segment and stacked over all segments. The CCFs between reference station #1 and other individual stations are shown in Figure 4. Rayleigh waves are evident and have a consistent pattern of propagation in the retrieved cross-correlation function.

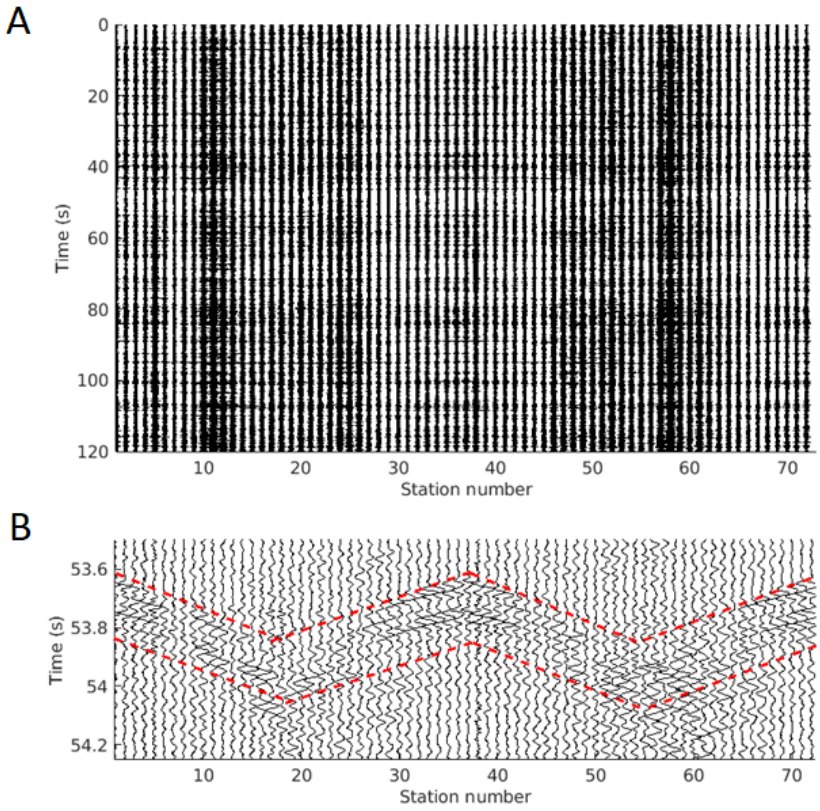

Figure 3. Miami highway bridge site: a) a sample noise record with many traffic-induced seismic events. b) close-up look (0.8 second long) between 53.5 s to 54.3 s of the data shown in a). A recorded surface-wave event is highlighted with red dash lines.

For inversion, the source time functions are estimated from the experimental CCFs using the deconvolution method (Wang et al. 2021). The initial PSD model (Figure 5) was established by observing the CCFs (Figure 4). As the signals with negative lag (time < 0) are dominant, suggesting dominant surface wave signals are from the left of the receiver array. The initial Vs

was established via analyzing the retrieved CCFs (Figure 4) presenting an apparent Rayleigh wave velocity of about 600 m/s. The velocity is high at the surface because the soil has been consolidated during highway construction. Assuming that the Rayleigh wave velocity is 85% of Vs, the initial Vs was taken as a homogeneous model with Vs=700 m/s.

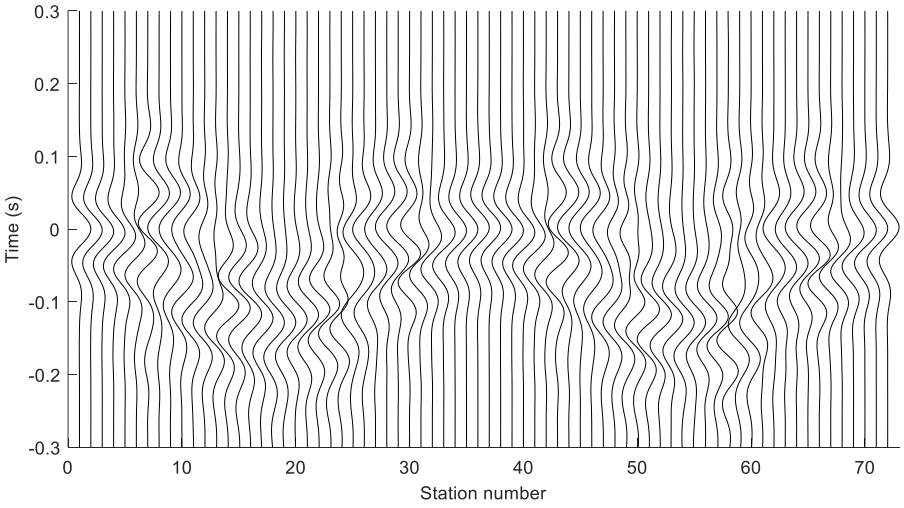

Figure 4. The retrieved cross-correlation function at the reference station #1.

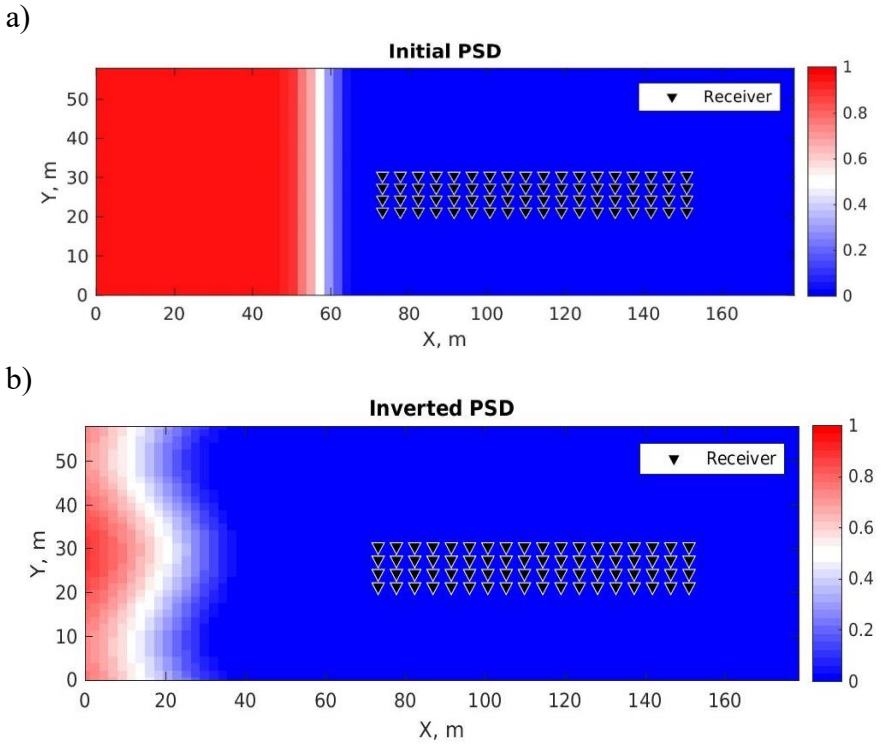

Figure 5. Source power spectrum density (PSD): a) initial and b) inverted. Black triangles represent receivers on the boundary of the sensor patch. The color bar displays normalized PSD magnitude.

The velocity model is set as 178 m × 58 m × 60 m (525 ft × 190 ft × 195 ft; X × Y × Z) and discretized into 40 × 20 × 14 cells (X × Y × Z). Each individual cell's dimension is 4.572 m × 4.572 m × 3.048 m (15 ft × 15 ft × 10 ft). The receiver patch is near the model's center with the receiver X-locations from 77 m to 155 m, and the receiver Y-locations from 24 m to 36 m (Figure 5a, black triangles). The center of the void is near the center of receiver array. This setting allows the modeled area to cover a length that is over 100 m longer than the geophone spread in X, benefiting the noise source distribution estimation.

The inversion was run for a total of 60 iterations, updating PSD for 10 iterations and updating Vs for 50 iterations. Specifically, the PSD was updated in iterations 1 to 5, and 16 to 20, and Vs was updated in remaining iterations. During inversion, Vp was updated as twice the value of Vs, and ρ was fixed to 1,800 kg/m3.

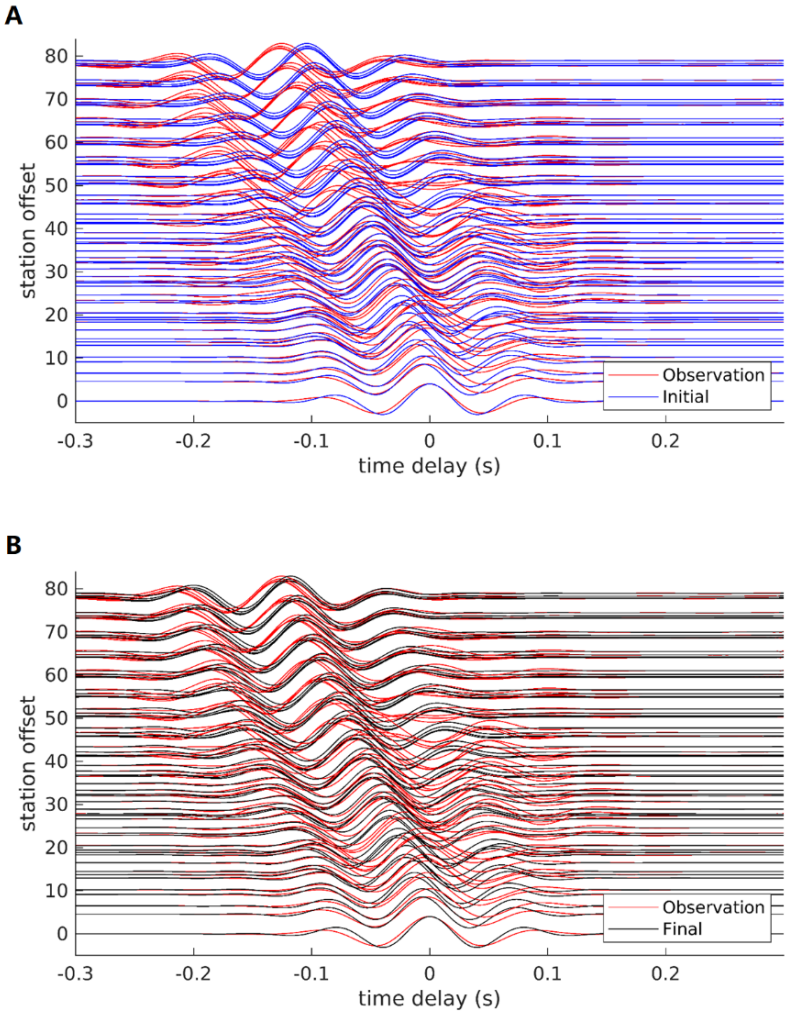

Figure 6. Miami highway bridge site, on reference station #1: a) Comparison of the observed cross-correlation function (red) with the first simulation (blue). b) Comparison of the observed cross-correlation function (red) with the final simulation (black).

The observed and simulated CCFs are compared in Figure 6. The comparison is carried out for reference station #1. At this station, the largest station offset is about 80 m. The red curves

are the observed cross-correlation function of traffic noise at 5-20 Hz. The blue and black dash curves are the initial and the final simulated cross-correlation functions, respectively. The waveform comparison shows that the overall fitting of the waveforms improved during the inversion. At the first iteration (Figure 6A), there is an evident gap of arrival-times between the observed and simulated CCFs. This difference in arrival time is caused by the large deep void. At the final iteration, the waveform match is considerably improved, and the arrival-time difference is small between the observed and simulated CCFs (Figure 6B). The normalized least-squares error is displayed in Figure 7. The error gradually decreases to about 56% from the first to final iteration, indicating that the final Vs model explains the data much better than the initial model.

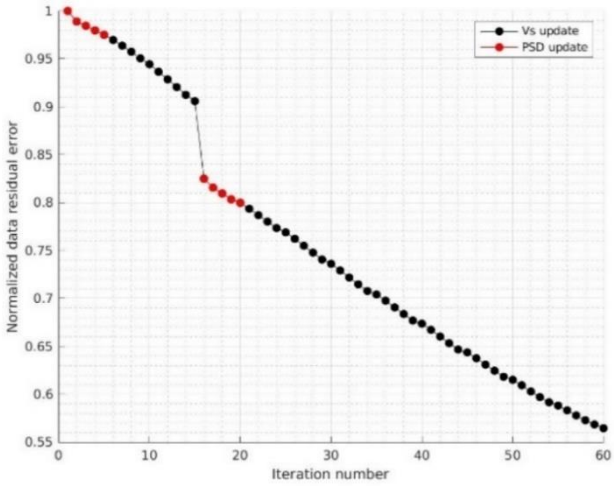

Figure 7. The normalized misfit error vs. iteration number.

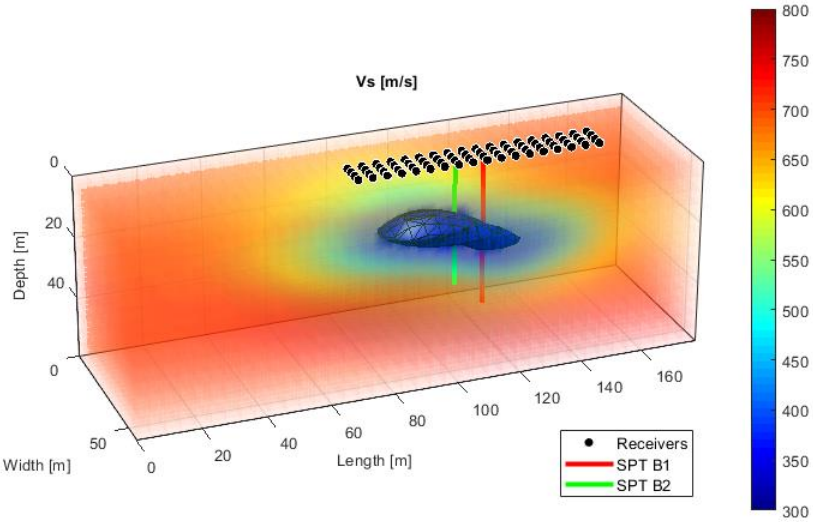

Figure 8. The inverted Vs model for the Miami bridge test site. The black cycles denote receivers on the surface. The blue object displays a collection of points with an equal value (350 m/s) in the inverted model. The red and green vertical lines denote the location of SPT tests B1 and B2, respectively. The color bar displays velocity in m/s.

The inverted PSD is shown in Figure 5b. This result indicates that ambient noise signals arrive mainly from the left of the receiver array (non-zero PSD). The inverted 3D Vs model is displayed in Figure 8. The blue object in this figure is an iso-surface, which represents the detected void. This iso-surface is a collection of points with an equal value (350 m/s) in the inverted Vs model. The inverted Vs shows a large void with Vs < ~300 m/s embedded in stiff materials. The center of the void is located at (x, y, z) = (114 m, 30 m, 30 m) with its height of about 25 m. The inverted Vs generally agree with the results of two SPTs (Figure 9), which show a large void from 28 to 44 m depth.

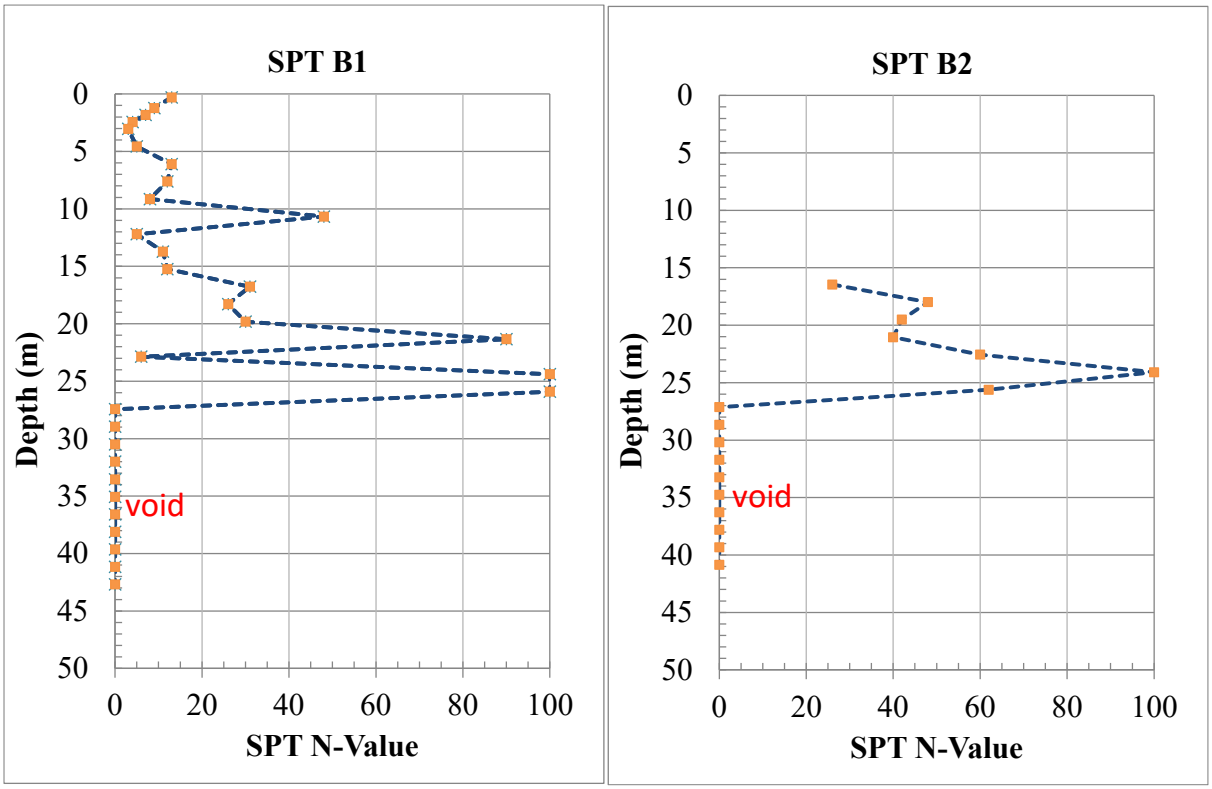

Figure 9: SPT results at locations B1 and B2 (refer to Figure 2)

CONCLUSION

This study investigates the capability of a newly developed 3D ambient noise tomography (3D ANT) method in detecting deep voids. The method was applied to an experimental noise dataset collected on top of a known deep void (28 to 44-m depth) in Miami, Florida. For the experiment, 72 vertical geophones were placed in a 2D surface grid of 9.0 m × 76.5 m to record traffic noises induced by passing vehicles. The cross-correlation functions (CCFs) extracted from the noise recordings are rich in low-frequency energy (5-20 Hz) and consistent in wave propagation pattern for the entire test area. By directly inverting CCFs to obtain Vs profile, the 3D ANT was able to image the void with accuracy. The characterized depth and vertical dimension of the void are generally consistent with invasive SPT results. Using ambient noise recordings with minimal field-testing effort, the 3D ANT is a useful technique for detecting large deep voids that are typically difficult to identify by active-source seismic methods.

ACKNOWLEDGMENTS

This work was supported by the National Science Foundation: grant CMMI-1930697. However, any opinions, findings, and conclusions or recommendations expressed in this material are those of the authors and do not necessarily reflect the views of the National Science Foundation.

REFERENCES

Barmin, M. P., M. H. Ritzwoller, and A. L. Levshin. 2001. A fast and reliable method for surface wave tomography, in *Monitoring the comprehensive nuclear-test-ban treaty: Surface waves*, Springer, 1351–1375.

Das, R., and S. S. Rai. 2016. Seismic interferometry and ambient noise tomography: theoretical background and application in south India: *Journal of Physics: Conference Series*, 759, 012006.

Di Giulio, G., C. Cornou, M. Ohrnberger, M. Wathelet, and A. Rovelli. 2006. Deriving wavefield characteristics and shear-velocity profiles from two-dimensional small-aperture arrays analysis of ambient vibrations in a small-size alluvial basin, Colfiorito, Italy: *Bulletin of the Seismological Society of America*, 96, 1915–1933.

Gutiérrez, F., I. Fabregat, C. Roqué, D. Carbonel, J. Guerrero, F. García-Hermoso, M. Zarroca, and R. Linares. 2016. Sinkholes and caves related to evaporite dissolution in a stratigraphically and structurally complex setting, Fluvia Valley, eastern Spanish Pyrenees. Geological, geomorphological and environmental implications. *Geomorphology* 267, 76-97.

Behm, M., N. Nakata, and G. Bokelmann. 2016. Regional ambient noise tomography in the Eastern Alps of Europe: *Pure and Applied Geophysics*, 173, 2813–2840.

Di Giulio, G., C. Cornou, M. Ohrnberger, M. Wathelet, and A. Rovelli. 2006. Deriving wavefield characteristics and shear-velocity profiles from two-dimensional small-aperture arrays analysis of ambient vibrations in a small-size alluvial basin, Colfiorito, Italy: *Bulletin of the Seismological Society of America*, 96, 1915–1933.

Endrun, B., M. Ohrnberger, and A. Savvaidis. 2010. On the repeatability and consistency of three-component ambient vibration array measurements: *Bulletin of Earthquake Engineering*, 8, 535–570.

Lin, F.-C., M. H. Ritzwoller, and R. Snieder. 2009. Eikonal tomography: surface wave tomography by phase front tracking across a regional broad-band seismic array: *Geophysical Journal International*, 177, 1091–1110.

Louie, J. N. 2001. Faster, better: shear-wave velocity to 100 meters depth from refraction microtremor arrays: *Bulletin of the Seismological Society of America*, 91, 347–364.

Moschetti, M. P., M. H. Ritzwoller, F. Lin, and Y. Yang. 2010. Seismic evidence for widespread western-US deep-crustal deformation caused by extension: *Nature*, 464, 885–889.

Mirzanejad, M., K. T. Tran, M. McVay, D. Horhota, and S. Wasman. 2021. "Deep void detection with 3D full waveform inversion of surface-based and in-depth source seismic wavefields" *Engineering Geology*, Vol. 294, 106407.

Nguyen, T. D., and K. T. Tran. 2018. Site characterization with 3D elastic full-waveform tomography: *Geophysics*, 83, R389–R400.

Mirzanejad, M., K. T. Tran, M. McVay, D. Horhota, and S. Wasman. 2021. Deep void detection with 3D full waveform inversion of surface-based and in-depth source seismic wavefields" *Engineering Geology*, Vol. 294, 106407.

Ritzwoller, M. H., F.-C. Lin, and W. Shen. 2011. Ambient noise tomography with a large seismic array: *Comptes Rendus Geoscience*, 343, 558–570.

Rosenblad, B. L., and J. Li. 2009. Comparative study of refraction microtremor (ReMi) and active source methods for developing low-frequency surface wave dispersion curves: *Journal of Environmental & Engineering Geophysics*, 14, 101–113.

Sager, K., L. Ermert, C. Boehm, and A. Fichtner. 2018. Towards full waveform ambient noise inversion: *Geophysical Journal International*, 212, 566–590.

Sager, K., C. Boehm, L. Ermert, L. Krischer, and A. Fichtner. 2020. *Global-scale full-waveform ambient*.

Schippkus, S., D. Zigone, G. Bokelmann, and A. W. Group. 2018. Ambient-noise tomography of the wider Vienna Basin region: *Geophysical Journal International*, 215, 102–117.

Tran, K. T., M. McVay, M. Faraone, and D. Horhota. 2013. Sinkhole detection using 2D full seismic waveform tomographySinkhole detection by FWI: *Geophysics*, 78, R175–R183.

Wang, Y., K. T. Tran, and D. Horhota. 2021. Road sinkhole detection with 2D ambient noise tomography: *Geophysics*, 86, KS123–KS135.

Wang, Y., M. Khorrami, K. T. Tran, and D. Horhota. 2023a. "Application of ambient noise tomography for deep void detection", *Journal of Applied Geophysics*, Vol. 209, 104922.

Wang, Y., K. T. Tran, B. Cox, and J. Vantassel. 2023b. "Geotechnical site characterization with 3D ambient noise tomography", *Geophysics*, Vol. 88 (4).

Wapenaar, K., and J. Fokkema. 2006. Green's function representations for seismic interferometry: *Geophysics*, 71, SI33–SI46.

Yang, Y., M. H. Ritzwoller, and C. H. Jones. 2011. Crustal structure determined from ambient noise tomography near the magmatic centers of the Coso region, southeastern California: *Geochemistry, Geophysics, Geosystems*, 12.

Youssef, A. M., Y. A. Zabramwi, F. Gutiérrez, A. M. Bahamil, Z. A. Otaibi, and A. J. Zahrani. 2020. Sinkholes induced by uncontrolled groundwater withdrawal for agriculture in arid Saudi Arabia. Integration of remote-sensing and geophysical (ERT) techniques. *Journal of Arid Environments* 177, 104132.